Influence of preferred orientation of clay particles on the diffusion of water in kaolinite porous media at constant porosity

Thomas Dabat[1]*, Patrice Porion[2], Fabien Hubert[1], Erwan Paineau[3], Baptiste Dazas[1], Brian Grégoire[1], Emmanuel Tertre[1], Alfred Delville[2], Eric Ferrage[1]*

[1] IC2MP-Hydrasa, UMR 7285 CNRS, Université de Poitiers, 86022 Poitiers, France

[2] ICMN, UMR 7374 CNRS, Université d'Orléans, 45071 Orléans, France

[3] Laboratoire de Physique des Solides, UMR 8502 CNRS, Université Paris-Sud, bât. 510, 91405 Orsay, France

Corresponding authors: thomas.dabat@univ-poitiers.fr; eric.ferrage@univ-poitiers.fr

Abstract

Solute transport in natural or artificial compacted clay porous media is receiving particular attention in the contexts of waste storage and the design of materials with tuneable physical properties. In these contexts, the porosity is commonly considered as a primary parameter controlling the diffusional properties of water and solutes in these systems. However, little attention has been given to the role played by anisotropy in the particle orientation. In this study, the influence of the preferred orientation of clay particles on the water diffusion anisotropy in two kaolinite porous media obtained by compaction and centrifugation methods (for a constant porosity value of ~0.5) was investigated by coupling experiments and simulations. An increase in the preferred orientation of kaolinite particles, as quantified by X-ray scattering analysis, was found to be logically associated with an enhanced anisotropy in water diffusion obtained from pulsed gradient spin echo attenuation measurements by nuclear magnetic resonance of protons. Brownian dynamics simulations performed on three-dimensional virtual porous media, mimicking the shape and orientation of the particles in the samples, led to calculated water diffusion coefficients in agreement with experimental data. Once validated, this computational work was extended to a wide range of degrees in the preferred orientation of particles. The results showed that this parameter leads to an increase and a decrease in pore water diffusion coefficients along and across the mean orientation plane, respectively, up to a factor ~2. The directional diffusion anisotropy was also found to range between 1 and ~5 for the most isotropic and anisotropic organisations, respectively. This study hence provides quantitative insights into the impact of the preferred orientation for the prediction of water diffusion in compacted clay media.

Keywords: clay minerals; porous media; anisotropy; particle orientation; water diffusion

1. Introduction

The understanding of solute transport in compacted clay-based porous media has considerable importance in the fields of nuclear waste storage in deep geological formations (Altmann et al., 2012; Charlet et al., 2017) and the design of innovative materials with fluid barrier efficiency (Aulin et al., 2012). For these systems, macroscopic transport models based on the Fickian expression of the diffusion process of a non-sorbing tracer rely on its effective diffusion coefficient D_e, defined by (Bourg et al., 2006; Tournassat and Steefel, 2015; Tinnacher et al., 2016):

$$D_e = \frac{\varepsilon}{G} D_0 \quad (1)$$

where ε is the porosity of the porous medium, D_0 the diffusion coefficient of the tracer in bulk liquid water, and G the tortuosity factor related to the geometry of the pore network. The diffusion coefficient of the tracer D in the pores, related to this D_e entity by $D_e = \varepsilon . D$, is thus expressed as follows:

$$D = \frac{1}{G} D_0 \quad (2)$$

In Eq. (2), all information regarding the geometry of the pore network, including the distributions in the size, shape, orientation, and connectivity of the pores, is contained in the entity G. Although different experimental methods such as microscopy techniques can be used to access specific properties of the porous network (Keller et al., 2014; Gaboreau et al., 2016; Leu et al., 2016; Backeberg et al., 2017; Takahashi and Tachi, 2019), the quantitative prediction of the geometric factor G value for a given porous medium remains a challenging task in the field of macroscopic transport modelling.

Because of their lamellar shape, clay particles most often display a preferred orientation, leading to anisotropy in the morphology of the pore network and having a considerable impact on the transfer properties of water and solutes. For instance, experimental studies have evidenced a significant variation in the measured water effective diffusion coefficients in the

direction parallel or perpendicular to the bedding of different natural argillaceous rocks (Van Loon et al., 2004; García-Gutiérrez et al., 2006; Xiang et al., 2013; Gimmi et al., 2014; Jacops et al., 2017). Furthermore it was also demonstrated that the increase in the diffusion anisotropy was qualitatively linked to a more pronounced preferred orientation of clay particles in the different samples (Wenk et al., 2008). Although the quantitative correlation between the water diffusion and porosity parameter has been subjected to a large number of studies (Van Loon and Mibus, 2015; Charlet et al., 2017 and references therein), little is known regarding the quantitative impact of the degree of preferred orientation on the diffusional properties of water and solutes. To obtain a complete understanding of this specific contribution, additional work on samples of model clay porous media with controlled porosity and anisotropic properties in the particle orientation is required.

In that context, the present study focuses on the water diffusion properties in two model porous media prepared from KGa-2 kaolinite particles with similar porosity but different particle orientations. The quantitative measurement of preferred orientation of the particles in these samples will be performed using X-ray scattering (XRS) analysis. An experimental analysis of the anisotropy in the water diffusion will be performed using pulsed gradient spin echo attenuation measurements by nuclear magnetic resonance (PGSE-NMR) of protons. Information regarding the particle size, shape and orientation will then be used to build 3D virtual porous media, for which Brownian dynamics simulations will be performed to analyse the water diffusional properties in the pore network. This computational methodology was recently shown to be efficient in connecting the different time scales of the diffusional process of water and solutes in compacted clay porous media (Tyagi et al., 2013; Bacle et al., 2016). Once validated against experimental data, the computational methodology will be extended to a wide range of degrees in preferential orientation of particles. The obtained results will

89 eventually help us to obtain quantitative insights into the role played by the preferential
90 orientation in the variation of the diffusional properties in these systems.

91 **2. Materials and methods**

92 *2.1. Starting material*

93 The kaolinite KGa-2 from the Source Clay Repository of the Clay Mineral Society was used
94 to prepare the different porous media. The average size of kaolinite particles is approximately
95 0.5 µm (Hassan et al., 2005) and their structural formula is
96 $[(Al_{3.80}Ti_{0.13}Fe^{3+}_{0.07})\ (Si_{3.84}Al_{0.16})\ O_5(OH_4)]$ (Mermut and Cano, 2001). The original kaolinite
97 powder was Na-saturated using three saturation cycles in a 1 mol/L NaCl solution to obtain
98 homoionic samples. Dialysis in deionised water was then used to remove the excess salt until a
99 silver nitrate test for Cl^- was negative. Finally, the kaolinite dispersion was dried in an oven at
100 60°C and then sieved through a 50 µm mesh to remove coarse aggregates.

101 *2.2. Preparation of porous media with contrasted anisotropy*

102 Two porous media made of kaolinite powder were prepared in order to obtain a similar
103 porosity value ε but contrasted anisotropy degrees in particle orientation. The first sample was
104 obtained by uniaxial compaction of the initial powder in a poly(tetrafluoroethylene) (PTFE)
105 cylinder with a diameter of 0.64 cm and a height of 7.5 cm. The kaolinite powder was
106 introduced in the tube, the tube placed in a metallic cell with a bottom cap to prevent widening,
107 and the powder then compressed to end up with a compacted kaolinite sample of 1 cm in height.
108 The second sample was obtained by a centrifugation process directly in the PTFE tube placed
109 in a poly(methyl methacrylate) (PMMA) cell to avoid deformation. To do so, the initial
110 kaolinite powder was first dispersed in water (50 g/L). A 1 mL aliquot of the obtained dispersion
111 was then introduced in the PTFE tube and centrifuged horizontally at approximately 18 000 g
112 (Centrifuge Avanti J 301 and rotor JS-24.38 from Beckman Coulter) for 10 min. After
113 centrifugation, the excess of water was removed before the addition of a new dispersion aliquot.

Ten steps were sufficient to obtain a sufficient amount of kaolinite material. Finally, the sample was dried at 60°C and slightly compressed to a 1 cm height using the same protocol as for the first sample.

The final bulk porosity ε of 0.45±0.02 for both samples was determined based on the weight of the samples (488±1 mg in both cases), their height (measurement after compression: 1.0 to 1.1 cm), and the kaolinite grain density. This latter value was estimated at 2.62 $g.cm^{-3}$ based on the structural formula mentioned above and the crystal structure parameters defined by Sakharov et al. (2016) for KGa-2 kaolinite. Both samples were realised twice following exactly the same protocol. The first set of samples was used for quantifying the particle orientation using XRS measurements after sample induration (see Section 2.3). The second batch of sample was used for the PGSE-NMR attenuation measurements of protons to extract the self-diffusion tensor of the water probes (see Section 2.4).

2.3. Sample induration and X-ray scattering measurements

Both dried porous media were indurated and sliced to perform XRS measurements in transmission mode. For the induration, methyl methacrylate (MMA; $C_5H_8O_2$) resin was chosen because of its fluidity higher than that of water allowing it to quickly fill the porosity, its small molecular volume compared to other organic molecules (19 nm^3), and its dipole moment being similar to that of water. The protocol used was based on the work of Sammaljärvi et al. (2012). The first step consists of setting the sample under a primary vacuum in a hermetic cell for few minutes. This step is necessary to fully dehydrate the sample, as water molecules can disturb the polymerisation reaction of MMAwihtout impacting their orientation (Hubert et al., 2013). In the second step, MMA mixed with benzoyl peroxide (BPO; added in a BPO/MMA ratio of 0.5 wt.% as a thermal initiator of the polymerisation) is introduced in PTFE tubes under vacuum to facilitate the vaporisation of MMA and its condensation into the smallest pores to fill all the porosity. For both preparation conditions (compacted and centrifuged samples), the saturation

of porosity by the resin was achieved after 3 days. The third step, consisting of the polymerisation of the MMA into PMMA, was achieved by transferring the saturated sample contained in the waterproof PTFE tube into a water bath at 55°C for 24 h.

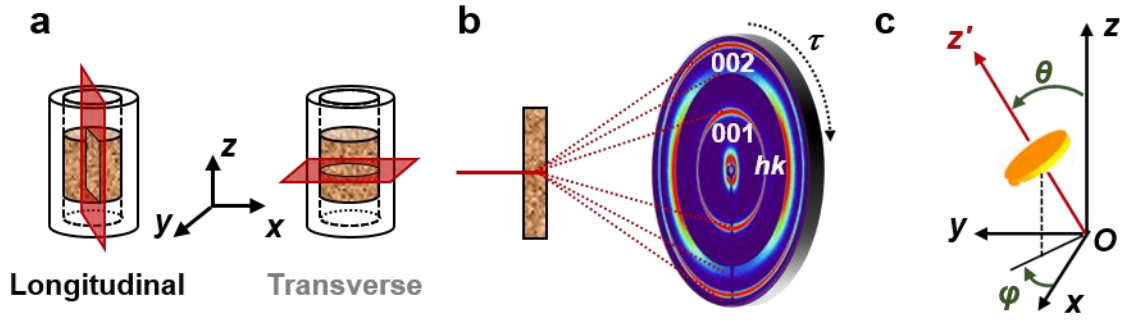

Fig. 1. Experimental measurement of particle orientation within kaolinite porous media using X-ray scattering technique with a 2D detector. (**a**) Sketches of the 500 µm-thick longitudinal and transverse lamellas relative to the tube axis and extracted from indurated samples to characterise the particle orientations. (**b**) Schematic representation of 2D-XRS measurements of lamellas in transmission mode. The modulation of the *hkl* Bragg reflection intensity rings along the detector angle τ is used to probe the particle orientation. (**c**) Spherical coordinates (θ, φ) defining the orientation of the normal (Oz') of an individual particle with respect to the laboratory frame (x,y,z).

After induration, the cylindrical porous media were extracted from the PTFE tubes and sawed in both the longitudinal and transverse directions of the tube axis (Fig. 1a). These two directions were chosen to investigate the particle orientation in the two main directions relative to the compaction/centrifugation forces. The obtained slices were then polished into 500 µm thickness lamellas using grinding paper (with a grain diameter of 5 µm). The XRS measurements were performed at the Laboratoire de Physique des Solides (Orsay, France). A copper rotating anode generator (RU H3R, Rigaku Corporation, Japan) equipped with a multilayer W/Si mirror (Osmic) allows obtaining a monochromatic beam ($\lambda_{CuK\alpha}$ = 1.5418 Å) of 600 x 600 µm² at the sample position. Two-dimensional (2D) X-ray scattering patterns were collected on a MAR345 2D-detector (marXperts GmbH, Germany, 150 μm pixel size). The

sample-to-detector distance D was set to 250 mm with a sample-to-beam stop distance of 30 mm. This configuration allows us to obtain scattering vector moduli down to Q_{min} = 0.2 Å^{-1} ($Q = 4\pi/\lambda \sin(\theta_B)$, where λ is the incident wavelength and $2\theta_B$ is the scattering angle), i.e., d-spacings up to 31.5 Å ($d = 2\pi/Q$). Sample lamellas were mounted on a goniometer head and aligned perpendicularly to the incident X-ray beam with a typical exposure time of 300 to 900 s per sample position (Fig. 1b). For the XRS analyses, the limited thickness of the lamellas (i.e., 500 µm) is a compromise to optimise both the percentage of the transmitted beam and the quantity of particles analysed over a 600 x 600 µm² surface.

2.4. ^{1}H NMR Pulsed Gradient Spin Echo experiments

The PGSE-NMR analyses were performed at the ICMN laboratory (Orléans, France). The dried kaolinite samples in their PTFE tubes (see Section 2.2) were first water-saturated by adding successive small drops of deionised water followed by equilibration over 2-3 days. As the samples were hydrated in unconstrained conditions, a limited decompaction occurred for both samples, leading to ε values increasing from 0.45±0.02 to 0.50±0.02, a final value confirmed by helium pycnometry (Porion et al., 2018).

The NMR measurements were performed using a Bruker DSX100 spectrometer with a static field of 2.35 T, equipped with a saddle detection coil and a micro-imaging probe (Micro5 Bruker) with gradient coils able to generate magnetic field gradients in three perpendicular directions. ^{1}H PGSE-NMR attenuation measurements (Stejskal and Tanner, 1965; Cotts et al., 1989; Callaghan, 1991) were used to determine the macroscopic water mobility along any pre-selected direction within the sample.

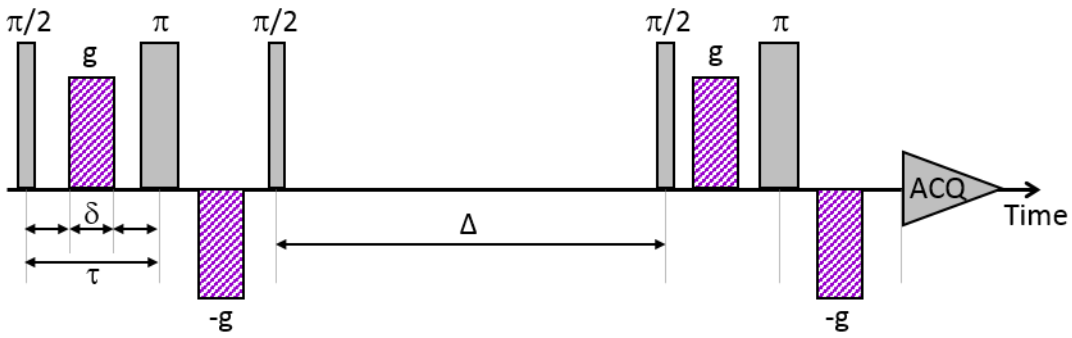

Fig. 2. Schematic view of the pulse sequence used to perform Pulse Gradient Spin Echo (PGSE-NMR) attenuation measurements. Details on the time delays, pulse durations and strengths of the magnetic field gradients are given in the text.

Fig. 2 illustrates the pulse sequence used to perform the PGSE-NMR attenuation measurements with which a wave vector q may be associated (Callaghan, 1991) according to the relationship $q = \gamma\, g\, \delta/\, \pi$, where g is the intensity of the applied field gradient (between 0 and 1.6 T/m), 2δ its effective duration (1 ms) and γ the proton gyromagnetic ratio (2.6752×10^8 rad/s for ^{1}H). With the fixed duration δ of the pulsed field gradient set equal to 500 µs, the maximum value of the probed wave vector reaches 6.8 10^4 m^{-1}. As a consequence, our diffusion measurements are macroscopic and result from averages over sample sizes larger than 15 µm with respect to the particle size (~0.5 µm). Under such macroscopic conditions (Porion et al., 2003), the attenuation of the intensity of the NMR echo $I(q)/I(0)$ evolves according to a Gaussian relationship from which the components of the self-diffusion tensor are easily extracted (Cotts et al., 1989; Callaghan, 1991):

$$\frac{I(q)}{I(0)} = exp\left[-4\,\pi^2\, q^2\, \overrightarrow{e_g}^T\, \overleftrightarrow{D}\, \overrightarrow{e_g}\, (\Delta + 3\tau/2 - \delta/6)\right] \quad (3)$$

where $\overrightarrow{e_g}$ is the direction of the applied field gradient and $\overleftrightarrow{D}$ the self-diffusion tensor. This equation is usually simplified by replacing the tensorial contraction $\overrightarrow{e_g}^T \overleftrightarrow{D}\, \overrightarrow{e_g}$ by the value of the self-diffusion coefficient D_g along the selected $\overrightarrow{e_g}$ director. The diffusion time Δ (20 ms) and the delay τ (760 µs) are also displayed in Fig. 2. The PGSE-NMR attenuation

measurements were performed at 292 K and the associated experimental bulk water self-diffusion coefficient D_0 was measured at $2.0 \pm 0.2.10^{-9}$ m^2/s in these conditions.

2.5. Generation of 3D virtual kaolinite porous media and Brownian dynamics

2.5.1. Simulated porous media of kaolinite with contrasted anisotropy and controlled porosity

The 3D virtual porous media (VPM) mimicking the organisation of kaolinite porous media for different degrees of anisotropy in particle orientation were obtained using a one-by-one deposition algorithm of elliptic disc-shaped particles (Ferrage et al., 2015, 2018). This type of simulation was recently shown to be able to reproduce the organisation and porosity of disc-shaped particle packings (Dabat et al., 2018). According to this algorithm, each particle with a set of Euler angles (φ, θ, ψ) following the *ZXZ* convention (Ferrage et al., 2015), is introduced at the top of a square simulation box with periodic conditions along the *x* and *y* axes (z axis pointing upward; Fig. 3a) and settles to provide the steepest descent of the barycentre altitude. The settling process of the particle, either at the bottom of the box or onto an existing bed of particles with fixed positions, is thus obtained through the repetition of individual movements around one or several contact points with one (or several) particles. The movements allow the particle to slide, swivel or rotate with a random amplitude ranging from zero to a maximum value to provide the steepest descent of the particle altitude. The variable parameters for the each simulation thus include a total number of particles (10 000), a width for the square simulation box set at $15\tilde{d}$, with $\tilde{d}$ the mean particle diameter, a total number of movement attempts (2400), an initial angle θ_{ini} of the particle introduced in the box, and a set of maximum amplitudes to swivel (A_{swiv}^{max}), to rotate (A_{rot}^{max} with here $A_{rot}^{max} = A_{swiv}^{max}$), and to slide ($A_{slide}^{max}$) (Ferrage et al., 2015). For these simulations, the lognormal distribution in the geometric dimensions (i.e., basal surface, particle diameter, ratio between thickness and diameter, and

ellipticity degree) of the individual elliptic particles was obtained from the work (Ferrage et al., 2015) and based on the experimental morphological study of Reinholdt et al. (2013) for the 0.1-0.2 µm size fraction of vermiculite from Santa Olalla, Spain. This vermiculite sample was used here as a proxy, because it displays particles having very similar average aspect ratios (i.e., ratio between thickness and diameter of particles) to that of KGa-2 kaolinite (0.08 and 0.07 for vermiculite and kaolinite, respectively; Hassan et al., 2005, Reinholdt et al., 2013).

The degree of anisotropy of particle orientation in the obtained packings was extracted by calculating the average of the second-order Legendre polynomial on the angular distribution of the particle orientations as follows:

$$\langle P_2 \rangle = \langle P_2(cos\theta) \rangle = \langle 3cos^2\theta - 1 \rangle / 2 \quad (4)$$

with θ the angle between the normal unit vector of the particle and the z axis of the simulation box (Figs. 1c and 3a). This $\langle P_2 \rangle$ order parameter takes the value of 0 for an isotropic organisation and 1 when all particles are perfectly oriented in the bedding (all normal to particles aligned with the z axis of the simulation box). The $\langle P_2 \rangle$ order parameter was previously used for the description of compacted clay porous media (Perdigon-Aller et al., 2005; Ferrage et al., 2015; Dabat et al., 2018) but is also referred to as H, the Hermans parameter in polymer sciences (Hermans and Platzek, 1939), or S, the nematic order parameter in colloid science (Chaikin and Lubensky, 1995; Davidson et al., 1995). To cover a large range of anisotropy degrees, 12 particle packings with $\langle P_2 \rangle$ values varying from 0.03 to 0.92 were generated according to algorithm parameters reported in Table S1.

To allow investigating the dynamic behaviour of water tracers in these different VPM, additional numerical treatments are necessary. The generation procedure of these VPM indeed leads to different porosity values as a function of the $\langle P_2 \rangle$ values (Ferrage et al., 2015; Dabat et al., 2018) and does not allow obtaining periodic conditions in the z direction. These effects are negative drawbacks for both Brownian dynamics calculations and comparisons with

experimental data on compacted/centrifuged kaolinite samples. To overcome these limitations, a specific methodology was employed for the most isotropic VPM constituted by approximately 10 000 particles, as illustrated in Fig. 3. Each individual particle, originally defined by a set of three parameters (thickness and major and minor axes), is first polygonised considering 12 in-plane vectors plus 2 vectors passing along the normal of the particle (Fig. 3b). A cubic sub-volume containing ~2000 particles is then extracted (Fig. 3c). In order to allow the numerical investigation of water tracer mobility over a large spatial domain, periodic conditions under the form of minimum-image convention along the directors $\overrightarrow{e_x}$, $\overrightarrow{e_y}$, and $\overrightarrow{e_z}$ are required for the newly obtained simulation box (Fig. 3d). For Brownian dynamics simulations this convention indeed insures that a water tracer passing through one side of the box will re-appears on the opposite side of the simulation box. However, it requires avoiding the case where a particle protruding out of one side could overlap on the other side of the box. This is achieved by first detecting particle overlapping after application of minimum-image convention along the directors $\overrightarrow{e_x}$, $\overrightarrow{e_y}$, and $\overrightarrow{e_z}$ and its removal by reducing the length of the different vectors defining the geometry of the two overlapping particles. The two following numerical treatments consist of reducing the porosity of the VPM in order to reach an ε value close to that of the water-saturated kaolinite samples analysed by PGSE-NMR, i.e., $\varepsilon = 0.50$ (see Section 2.4). First, each particle is allowed to grow along one of its 14 vectors, chosen randomly. The amplitude of the increase in the vector length is also chosen randomly between zero and a maximum value set at 10% of the initial vector length. In the case where the modification of the particle geometry induces an overlapping with another particle of the packing, the attempt is rejected. This first procedure allows increasing the volume of solid in the packing and thus decreasing the porosity until all particles become geometrically constrained by the other particles from the stack (Fig. 3e). Second, if the porosity obtained still remains higher than the target value, new solid volume is added by injecting a new particle into the stacking on the surface of an existing one and letting

the particle grow along its 14 vectors (Fig. 3f). The newly injected particles satisfy the distribution of the geometric dimensions but only the addition of the smallest ones is likely to be accepted during such a procedure. Depending on the initial porosity of the original VPM, the procedure is stopped during either the first or the second treatment, i.e., when the VPM reaches the porosity of ε=0.50. Note that if the porosity is the same for all VPM, these two processes lead to a modification in the particle sizes and thus a change in the overall specific surface areas (SSAs). For instance, an increase in the volume of the individual particles leads to a decrease in the SSA values, whereas the injection of new particles, most often small in size, in order to fill the remaining porosity leads to an increase in the SSA values. Accordingly, the final step of the VPM generation procedure thus consists of applying a dilatation or contraction of the overall packing (and thus particle) dimensions (Fig. 3e). This leads to VPM with cubic lengths of ~4 μm (i.e., between 4.3 and 3.9 between $\langle P_2 \rangle$=0.03 and 0.92, respectively) and SSA values of ~20 m^2/g (similar to the experimental SSA value for KGa-2 kaolinite; Hassan et al., 2005).

2.5.2. Brownian dynamics of water in virtual porous media

Brownian dynamics (BD) simulations represent a convenient way to investigate water diffusion at the representative time scale of the micrometre-sized porous media (typically several ms). In the framework of the general Langevin equation, the displacement of the molecular probes can be defined by (Gunsteren et al., 1981; Tertre et al., 2015; Porion et al., 2018):

$$m_i \frac{d\vec{v}_i(t)}{dt} = -m_i \gamma_i \vec{v}_i(t) + \vec{F}_i(x(t), t) + \vec{R}_i(t) \quad (5)$$

where $\vec{v}_i$, m_i and γ_i are the velocity, molecular mass and frictional coefficient of probe i, respectively, $\vec{F}_i(x(t), t)$ is a systematic force acting on the probes and depending on their positions and $\vec{R}_i(t)$ is a random force resulting from thermal collisions within the liquid. Different algorithms can be used to solve the set of Eq. (5), mainly depending on the ratio

between the friction coefficient and the time step (δt) used in the simulation. In the case where the time step is much larger than the velocity correlation time (i.e., $\gamma_i \delta t \gg 1$) and considering the probe displacements to be completely independent, the solution of Eq. (5) becomes (Gunsteren et al., 1981):

$$\vec{x}_i(t + \delta t) = \vec{x}_i(t) + \vec{R}_i \tag{6}$$

with the random force $\vec{R}_i$ now satisfying a Gaussian distribution function with a zero mean and standard deviation given by the following:

$$\langle {R_i}^2 \rangle = 2 D_i \delta t \tag{7}$$

where D_i is the molecular self-diffusion of the probe i. For diffusion within isotropic media, the modulus of the random 3D displacements is quantified by the self-diffusion propagator, i.e., the density of the probability of the displacement distribution law (Callaghan, 1991; Bacle et al., 2016):

$$P(\vec{r}, \Delta \mid \vec{r}_0 \ ,0) = \{4\pi D \Delta\}^{-3/2} exp\left[-\frac{(\vec{r}-\vec{r}_0)^2}{4D\Delta}\right] \tag{8}$$

where Δ is the diffusion time (see Eq. (3)). The self-diffusion propagator quantifying the mobility along any single director is then defined by the following:

$$P_\alpha(\overrightarrow{r_\alpha}, \Delta \mid \overrightarrow{r_{\alpha_0}}, 0) = \{4\pi D_\alpha \Delta\}^{-1/2} exp\left[-\frac{\left(\overrightarrow{r_\alpha}-\overrightarrow{r_{\alpha_0}}\right)^2}{4D_\alpha \Delta}\right] \tag{9}$$

where D_α is the component of the self-diffusion tensor describing the mobility of the probe along the selected $\overrightarrow{e_\alpha}$ director (Callaghan, 1991). Its spatial Fourier transform is also Gaussian and describes the probe displacement in the reciprocal q-space:

$$E_\alpha\,(q, \Delta\,) = \exp\left[-2\,\pi^2\,q^2\ \langle\left(\overrightarrow{r_\alpha} - \overrightarrow{r_{\alpha_0}}\right)^2\rangle\right] = \ \exp[-4\,\pi^2\,q^2\,D_\alpha\,\Delta] \tag{10}$$

where Δ is the diffusion time and $\langle\left(\overrightarrow{r_\alpha} - \overrightarrow{r_{\alpha_0}}\right)^2\rangle$ the mean-squared displacement along the $\overrightarrow{e_\alpha}$ director (Callaghan, 1991; Porion et al., 2001, 2003). In the scope of comparing simulations and experiments, as done in the present study, it should be pointed of that this Fourier transform

of the self-diffusion propagator derived from BD simulations corresponds to the entity directly probed by PGSE-NMR measurements (see Section 2.4). Moreover it also corresponds exactly to the intermediate scattering function ($F_q(t)$) commonly probed, on a much shorter time-scale, by quasi-elastic neutron-scattering measurements (Hansen and McDonald, 1990).

For the BD simulations performed here at 300 K, N = 2500 water probes with the molecular self-diffusion D_0 set at 2.3.10^{-9} m^2/s were first introduced randomly into the porosity of the VPM. A time step δt = 5 ns was considered, and additional tests showed that smaller values did not provide any difference in the simulation results. An overall simulation time of 4 ms was used to extract the pore water diffusion coefficients D_α along a selected $\overrightarrow{e_\alpha}$ director based on the asymptotic slope of the radial mean squared displacement as follows:

$$D_\alpha = \lim_{\Delta \to \infty} \frac{\sum_{i=1}^{N} (x_{i,\alpha}(0) - x_{i,\alpha}(\Delta))^2}{2N\Delta} \quad (11)$$

where α refers to the single direction $\overrightarrow{e_\alpha}$ on which the mobility is extracted (the uncertainty on the calculated D_α values is estimated at 10%). During the BD simulations, the collision with the surface of the kaolinite was treated as a Maxwell's A wall with the angular probability $f_A(\theta, \phi)$ of water probes rebounding from the surface given by:

$$f_A(\theta, \phi) d\Omega = \cos\theta \, d\Omega / \pi \quad (12)$$

where θ and ϕ are the usual polar and azimuthal angles (with respect to the normal of the surface of the particle) and $d\Omega$ is the element of the solid angle. This condition mimics the fate of a molecule, which is supposed to reside at the interface of the wall and eventually leave the wall to return to the fluid (Valleau et al., 1991).

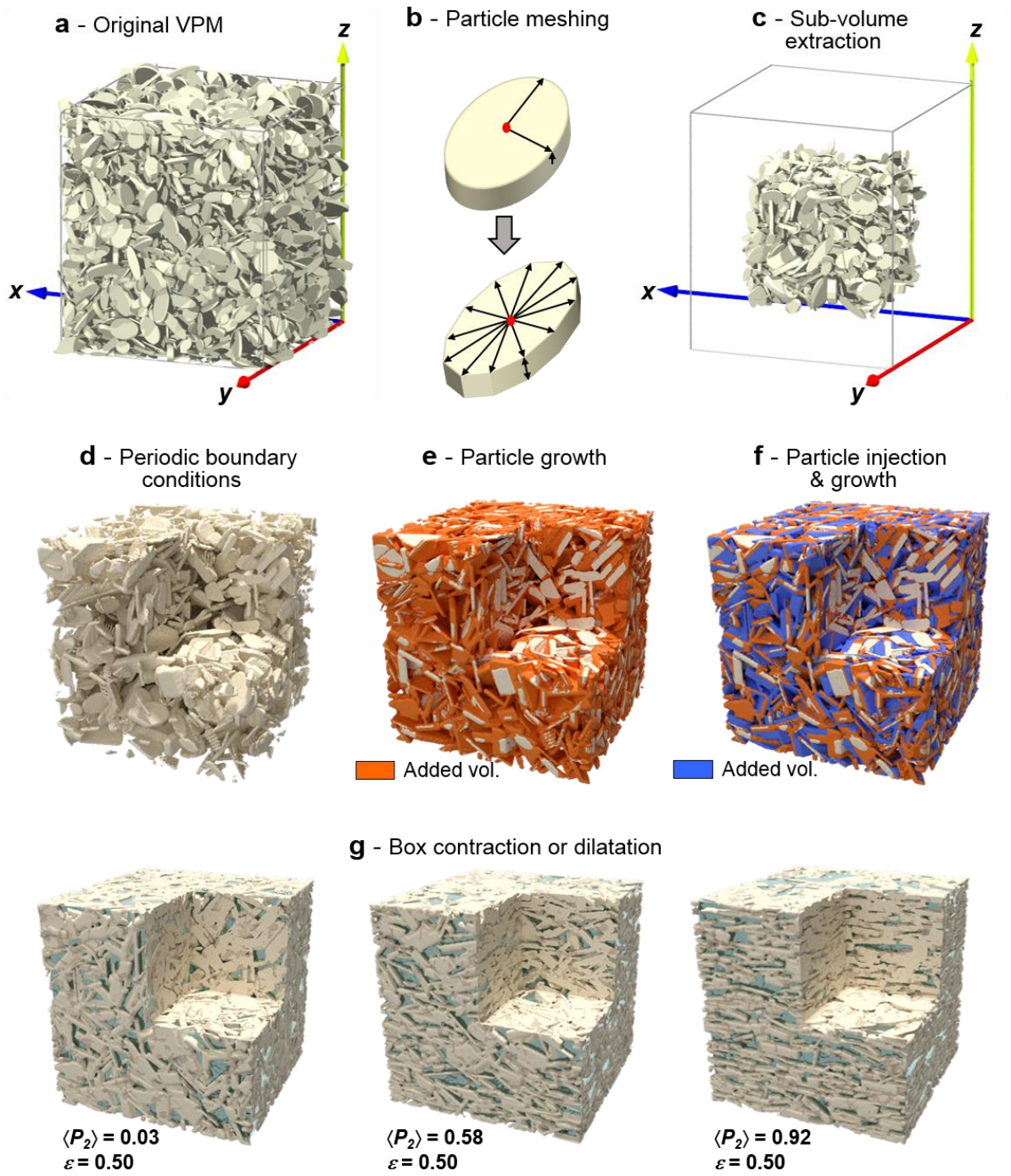

Fig. 3. Generation of virtual porous media with the same porosity but different anisotropy degrees in particle orientation. (**a**) Cubic 3D virtual porous medium composed of ~10 000 particles with an almost isotropic organisation ($\langle P_2 \rangle$ = 0.04) and generated using a sequential deposition algorithm (Ferrage et al., 2015, 2018). (**b**) Meshing and polygonalisation of individual particles. (**c**) Extraction of a cubic sub-volume with ~2000 particles. (**d**) Application of periodic boundary conditions along $\overrightarrow{e_x}$, $\overrightarrow{e_y}$, and $\overrightarrow{e_z}$ directors of the simulation box and elimination of particle overlapping. (**e**) Decrease of porosity by

particle growth along the 14 individual axes (12 and 2 axes on the basal surface and along the normal of the particle, respectively). (**f**) Decrease of porosity by injection of new particles and subsequent growth along their 14 individual axes. (**g**) Contraction or dilation of the overall 3D cubic porous media in order to keep the total specific surface area similar for all samples (VPM obtained for $\langle P_2 \rangle$ = 0.58 and 0.92 are also shown here for illustration).

3. Results and Discussion

3.1 Preferred orientation analysis of kaolinite particles

Preferred orientation of the particles in both the compacted and centrifuged samples is based on the orientation distribution function (ODF) determined from 2D-XRS measurements (see Section 2.3). The orientation of a cylindrical particle can be described in an orthogonal laboratory framework by the direction of its normal *Oz'* through the spherical coordinates θ and φ (Fig. 1c). In addition, clay porous media are transverse isotropic systems with their *z*-axis as the unique symmetry axis (Cebula et al., 1979; Perdigon-Aller et al., 2005; Wenk et al., 2010; Hubert et al., 2013), leading to an equal probability of the particle orientation over the φ angles. Accordingly, the ODF only depends on the angle θ, with the following general constraints:

$$f(\theta) \geq 0 \tag{13}$$

$$f(\theta) = f(\pi - \theta) \tag{14}$$

$$\int_0^{\pi} f(\theta) \sin(\theta)\, d\theta = 1 \tag{15}$$

Eqs. (13) and (14) indicate that the ODF $f(\theta)$ is positive and has an equal probability of the particles pointing upward and downward, respectively. Eq. (15) allows normalising the total number of particles in the system through the integration over all φ angles (Labarthet et al., 2000). The experimental ODF can be extracted from the angular modulation of the scattered intensity of the 001 reflection of kaolinite along the detector angle τ of the 2D-XRS patterns (Fig. 1b). Given the low values for the Bragg angle for the 001 reflection of kaolinite, the $\tau = \theta$

approximation can indeed be considered, and the $f(\theta)$ ODF is thus directly extracted from the scattered intensity $I(\theta)$ evolution:

$$f(\theta) = \frac{I(\theta)}{\int_0^{\pi} I(\theta)\sin(\theta)d\theta} \quad (16)$$

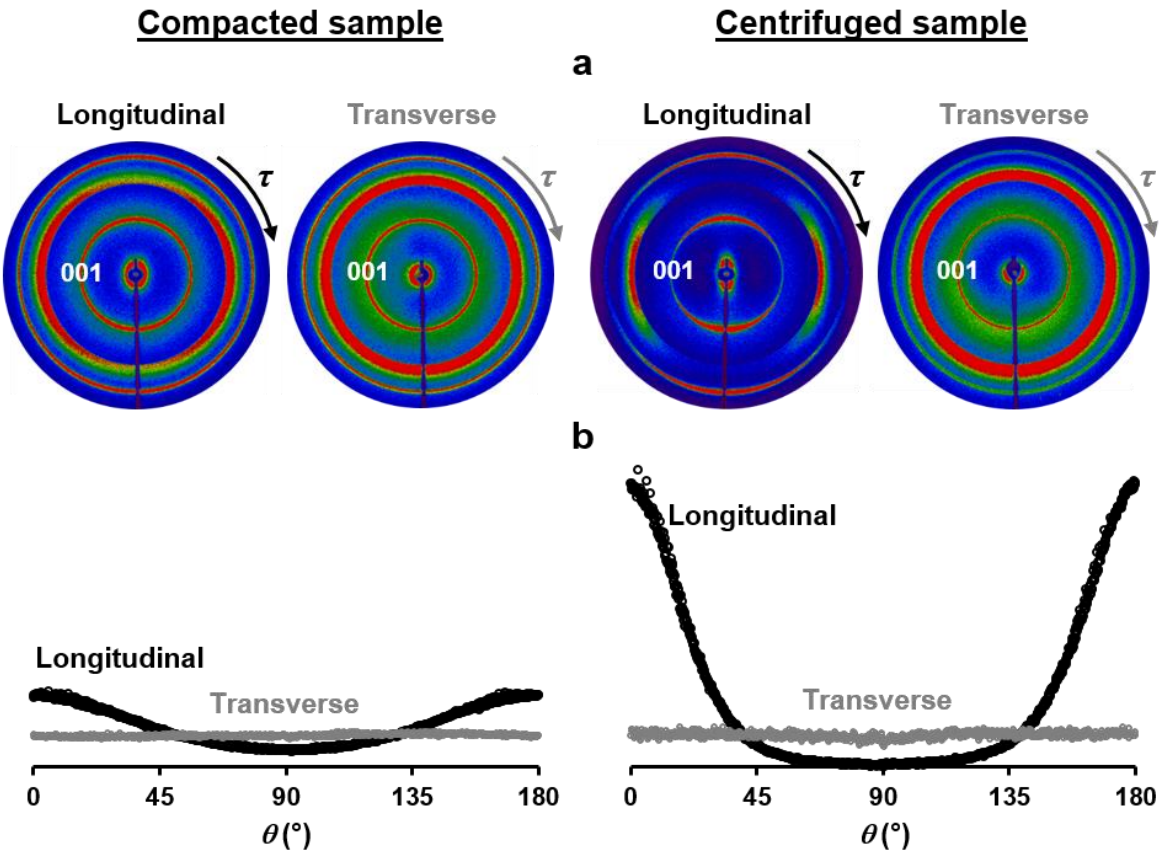

Fig. 4. Extraction of orientation distribution functions of kaolinite particles from 2D X-ray scattering measurements. (a) Experimental 2D-XRS patterns recorded from the compacted and the centrifuged samples in both the longitudinal and transverse directions of the tube axis. The colour scale ranges from dark blue for the smallest intensity values to red for the largest ones. (b) Corresponding orientation distribution functions from the angular scan of the 001 reflection of kaolinite over 180° (normalised intensity according to Eq. (15), resulting in the same intensity for isotropic ODF).

The experimental 2D-XRS patterns for both the compacted and centrifuged samples on lamellas extracted in the longitudinal and transverse directions with respect to the tube axis are reported in Fig. 4 with their corresponding ODF. As seen for both samples, the $f(\theta)$ functions recorded for the lamellas extracted in the longitudinal direction display symmetric profiles,

indicating that the lamellas were sliced perpendicularly to the preferred orientation plane and well aligned on the XRS setup. For lamellas corresponding to the transverse direction of the tube axis, the obtained ODF displays a constant intensity whatever the azimuthal angle, in agreement with the isotropic transverse nature of the sample and the correct methodology of the sample preparation and analysis. Based on the shape of the $f(\theta)$ functions for lamellas sliced in the longitudinal direction of the tube axis, the degree of preferred orientation can be obtained for both samples by calculating the average value of the second-order Legendre polynomial on the angular distribution as:

$$\langle P_2 \rangle = \int_0^{\pi} P_2(cos\theta).f(\theta)\sin(\theta)\,d\theta \quad (17)$$

As seen from the different shapes of the $f(\theta)$ functions (Fig. 4b), the two samples display very different order parameters, with $\langle P_2 \rangle$ values of 0.21±0.02 and 0.59±0.05 for the compacted and centrifuged samples, respectively (Table 1). It is worth noting that the obtained $\langle P_2 \rangle$ values are averages over several measurements for each sample. Although it can be expected that the successive centrifugation steps lead to a more heterogeneous sample organization, such a difference was not evident given the about 10% uncertainty of the structure parameter in both cases (Table 1). The different organisations for the two samples can likely be attributed to the preparation method for two reasons. First, the uniaxial compaction in air-dried conditions has been shown to provide rather poor preferred orientations for montmorillonite particles (Lutterotti et al., 2010; Suuronen et al., 2014). Second, it is well accepted that the dispersion of particle aggregates as individual clay platelets in water followed by sedimentation promotes the preferred orientation, and a wide range of $\langle P_2 \rangle$ values could be achieved, depending on the particle size, solid-solution ratio, and hydrostatic or shear forces applied on the sample ($0.10 \leq \langle P_2 \rangle \leq 0.85$; Perdigon-Aller et al., 2005; Méheust et al., 2006; Perdigón et al., 2007; Hubert et al., 2013; Ferrage et al., 2015; Carrier et al., 2016).

Table 1. Experimental measurements of the anisotropy degree of particle orientation (order parameter $\langle P_2 \rangle$) determined from XRS analyses and associated pore water diffusion coefficients D_α obtained from PGSE-NMR experiments on compacted and centrifuged samples (porosity ε=0.50±0.02). The director $\overrightarrow{e_z}$ is longitudinal whereas the directors $\overrightarrow{e_x}$ and $\overrightarrow{e_y}$ are transverse to the tube axis.

Sample	$\langle P_2 \rangle$ order parameter	D_z/D_0	D_x/D_0	D_y/D_0	$D_{\overline{x,y}}/D_z$
Compacted	0.21±0.02	0.43±0.04	0.51±0.05	0.50±0.05	1.2±0.2
Centrifuged	0.59±0.05	0.31±0.03	0.59±0.06	0.57±0.06	1.9±0.4

3.2 Experimental analysis of water diffusion in kaolinite porous media

The contrasted organisations in the kaolinite particles (i.e., $\langle P_2 \rangle$ = 0.21±0.02 and 0.59±0.05 for the compacted and centrifuged samples, respectively) for a similar porosity (ε = 0.50±0.02 in wet conditions; see Section 2.4) indicate that the two samples are well adapted to investigate in detail the impact of the preferred orientation on the anisotropy of the water diffusion. As illustrated in Fig. 5 for the centrifuged sample, the pulsed gradients are applied along six non-collinear directions (Basser et al., 1994; Skare et al., 2000) noted $\overrightarrow{e_1} = \overrightarrow{e_x} = (1,0,0)$, $\overrightarrow{e_2} = \overrightarrow{e_y} = (0,1,0)$, $\overrightarrow{e_3} = \overrightarrow{e_z} = (0,0,1)$, $\overrightarrow{e_4} = (1,1,0)$, $\overrightarrow{e_5} = (0,1,1)$ and $\overrightarrow{e_6} = (1,0,1)$, respectively, with the direction $\overrightarrow{e_3}$ being parallel to the compaction/centrifugation axis of the sample. From the six corresponding components of the water self-diffusion tensor, one can easily extract its three principal axes and the corresponding eigenvalues describing the water mobility in the longitudinal or transverse direction of the tube axis (Fig. 1a).

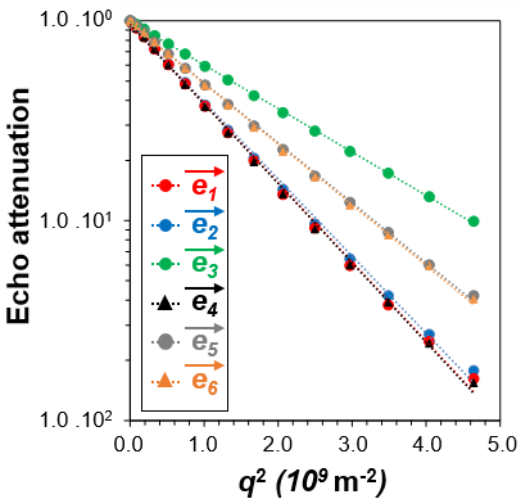

Fig. 5. Illustration of water self-diffusion propagators obtained for the centrifuged sample from PGSE-NMR experiments. More details on the selected diffusion directors $\overrightarrow{e_\alpha}$ are given in the text, leading to the components D_α of the self-diffusion tensor: D_1=D_x=1.142×10^{-9} m^2/s, D_2=D_y=1.165×10^{-9} m^2/s, D_3=D_z=0.614×10^{-9} m^2/s, D_4=1.173×10^{-9} m^2/s, D_5=0.869×10^{-9} m^2/s and D_6=0.879×10^{-9} m^2/s.

As detailed in Table 1, the compacted sample exhibits a small anisotropy of the water self-diffusion tensor, which is consistent with the measured low values for the order parameter $\langle P_2 \rangle$. Moreover, the pore water diffusion coefficient obtained for this sample along the *z* direction is consistent with a previous analysis from magnetic resonance imaging of the time evolution of the water concentration profiles during D_2O/H_2O exchange (Porion et al., 2018). In contrast, the sample obtained by the centrifugation method shows a larger anisotropy ratio $D_{\overline{x,y}}/D_z$ of the water diffusion tensor, in agreement with the increase of the $\langle P_2 \rangle$ order parameter value for this sample. The water self-diffusion tensor can be better illustrated for these two samples by plotting the variation of the water mobility within two orthogonal planes (i.e., either parallel or perpendicular to the preferred orientation plane). The gradual variation of the pore water diffusion coefficients between the two principal axes of the diffusion tensor (i.e., $\overrightarrow{e_\perp}$ and $\overrightarrow{e_\parallel}$, directions perpendicular or parallel to the preferred orientation plane, respectively) can indeed be described by (Porion et al., 2003):

$$D_{meas}(\gamma) = \overrightarrow{e_g}^T \overleftrightarrow{D} \overrightarrow{e_g} = D_\perp \cos^2(\gamma) + D_\parallel \sin^2(\gamma) \quad (18)$$

where γ is the angle between $\overrightarrow{e_\perp}$ and $\overrightarrow{e_g}$. D_α and $D_\parallel$ are the two eigenvalues of the diffusion tensor along the principal directions $\overrightarrow{e_\perp}$ and $\overrightarrow{e_\parallel}$. The diffusion tensor is illustrated in Fig. 6 for both the compacted and centrifuged samples. Calculations are performed either parallel or perpendicular to the preferred orientation plane based on the (*x*,*z*) or (*x*,*y*) planes, respectively.

The enhanced experimental anisotropy in the water mobility on the (*x*,*z*) plane for the centrifuged sample compared to the compacted sample well illustrates the role played by the preferred orientation of the kaolinite particles on the water mobility for a given ε value. In that regard, and compared to other diffusion experiment setups, the great advantage of the PGSE-NMR attenuation measurements is to provide a direct measurement of the water diffusion tensor in the sample. Such experimental data thus represent key constraints for assessing the representativeness of virtual porous media through a detailed comparison between the experimental and simulated water mobility dependences on the particle orientation.

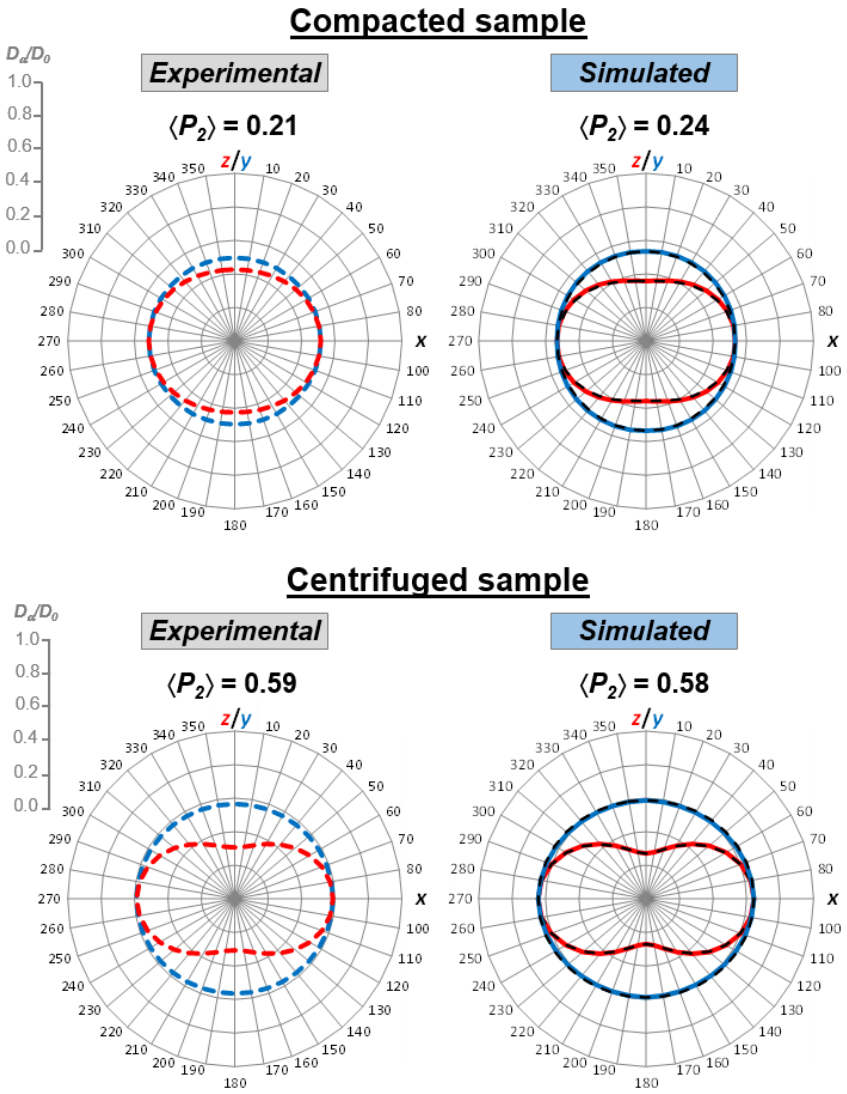

Fig. 6. Water diffusion tensors determined from PGSE-NMR experiments (left) and Brownian dynamics simulations (right). The variations of the water mobility D_α/D_0 in the (x,y) plane and (x,z) plane are shown in blue and red, respectively. For the experimental data, the diffusion tensor is calculated from its eigenvalues D_x, D_y, and D_z according to Eq. (18). For the simulated data, the solid lines correspond to the limiting time evolution of the mean square displacements (see Eq. (11)), whereas the dotted lines represent the calculation of the diffusion tensor from its eigenvalues using Eq. (18).

3.3 Brownian dynamics of water diffusion in 3D virtual porous media

The pore diffusion coefficients in the 12 virtual porous media (with $0.04 \leq \langle P_2 \rangle \leq 0.92$) are calculated along the 3 directors of the 3D virtual porous media reference framework (i.e., x, y, and z; Fig. 7) based on the mean square displacement (MSD) of the water probes according

to Eq. (11). Additional calculations were performed every 10° in the (*x*,*y*) and (*x*,*z*) planes of the diffusion tensor.

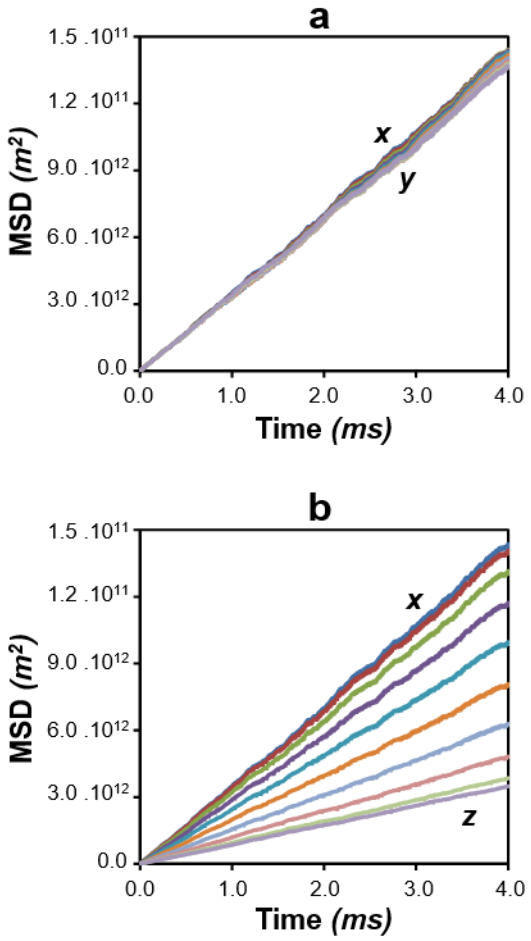

Fig. 7. Illustration of the time evolution of the mean square displacements (MSD) of the water probe obtained by Brownian dynamics simulations for the virtual porous media with $\langle P_2 \rangle$ = 0.92. Displacements are extracted along the 3 directors of the 3D virtual porous media reference framework (i.e., *x*, *y*, and *z*) as well as every 10° in the (a) (*x*,*y*) plane and (b) (*x*,*z*) plane.

As illustrated in Fig. 7 for the VPM obtained for $\langle P_2 \rangle$ = 0.92, the asymptotic time evolution behaviour of the MSD is rapidly obtained. The different MSD curves extracted in the (*x*,*y*) plane of the diffusion tensor are very similar (Fig. 7a). This feature confirms the transverse isotropy of the VPM, in agreement with the experimental data (see Section 3.1). Moreover, this lack of angular dependence of the calculated D_α values likely evidence that the VPM contain

sufficient numbers of particles and thus can be considered as representative elementary volumes for the analysis of the dynamical behaviour of diffusive species. The situation differs when analysing the MSD curves in the (*x*,*z*) plane of the diffusion tensor (Fig. 7b). The D_α values are indeed significantly lower in the *z* direction compared with the ones in the *x* direction, with intermediate values of D_α for in-between directions. This observation is consistent with the plane (*x*,*y*) as the preferred orientation plane.

The pore water diffusion coefficients D_α derived from these different MSD curves are used to draw the water diffusion tensor in Fig. 6 for the two VPM having the closest $\langle P_2 \rangle$ values to the experimental ones, i.e., $\langle P_2 \rangle$ = 0.24 and 0.58. The overall D_α values are found to be in fair agreement when comparing the experimental and calculated water diffusion tensors. For the compacted sample, the simulated tensor displays a slightly more anisotropic pattern, likely due to the increased $\langle P_2 \rangle$ value ($\langle P_2 \rangle$ = 0.24 and 0.21 for simulated and experimental media, respectively). In Fig. 6, the obtained simulated water diffusion tensor (solid line) is also compared to the tensor (black dotted line) only based on the extracted D_x, D_y, and D_z values from BD simulations and considering the angular dependence given by Eq. (18). The good consistency between the simulated and recalculated water diffusion tensors provides additional evidence of the good representativeness of the VPM as well as the correct consideration of the simulated $\overrightarrow{e_x}$, $\overrightarrow{e_y}$, and $\overrightarrow{e_z}$ directors of the simulation box as eigenvalues of the diffusion tensor. The obtained VPM coupled to BD simulations can be used to further assess the influence of the preferred orientation of particles on the diffusional properties of water. In Fig. 8a, the obtained simulated D_α/D_0 values extracted from the MSD curves are plotted in the 0.04-0.92 $\langle P_2 \rangle$ range, whereas the anisotropy ratio $D_{\overline{x,y}}/D_z$ of the water diffusion tensor is reported in Fig. 8b. Again, good agreement between the experimental and calculated diffusion coefficients is obtained for both samples. The $D_{\overline{x,y}}/D_0$ and D_z/D_0 values show steady increasing and decreasing behaviours, respectively, when increasing the degree of preferred orientation (Fig. 8a). For both

directions, a factor ~2 is obtained for G values between the more isotropic to more anisotropic systems. This amplitude observed for ε=0.5±0.02 is in agreement with the computational results obtained by (Tyagi et al., 2013) using random walk simulations on 2D microstructure maps. Such variation well illustrates the great importance of the preferred orientation on the diffusional properties of water. In the case of transport modelling, according to Eq. (1), the modification of the D_α/D_0 values through the investigated $\langle P_2 \rangle$ range has indeed the same impact on the D_e value as a change in the porosity value by a factor of 2.

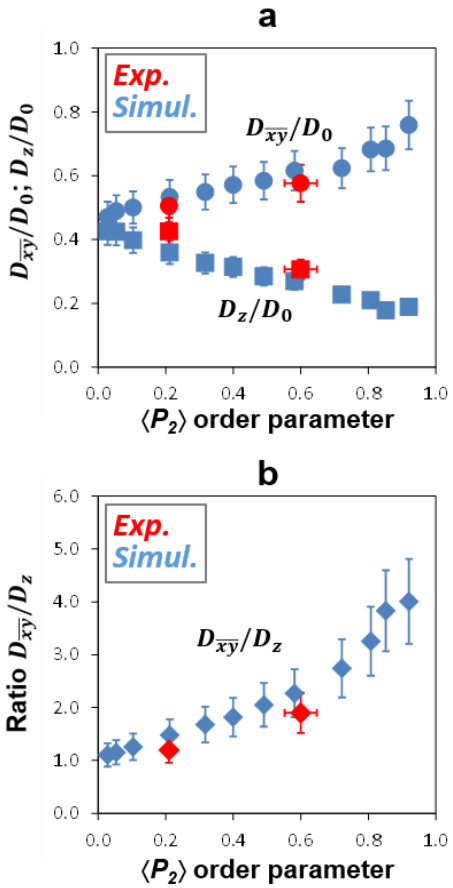

Fig. 8. Influence of particle preferred orientation on the water diffusion properties. (a) Evolution as a function of the order parameter $\langle P_2 \rangle$ of the mean water diffusion coefficients in the (*x*,*y*) plane $D_{\overline{x,y}}$ (circles) or along the *z* direction D_z (squares), calculated from Brownian dynamics simulations (blue) or obtained experimentally by PGSE-NMR attenuation measurements (red). (b) Evolution of experimental (red) and calculated (blue) $D_{\overline{x,y}}/D_z$ ratios with preferred orientation of particles.

The anisotropy ratio $D_{\overline{x,y}}/D_z$ of the water diffusion tensor displays an exponential-shaped evolution with the $\langle P_2 \rangle$ value (Fig. 8b). The observed variation of the $D_{\overline{x,y}}/D_z$ values between 1 and 5 is consistent with the reported experimental diffusivity anisotropies for water tracers in compacted clay-rich porous media, for pure clay-based materials (e.g., bentonite; Sato and Suzuki, 2003; Suzuki et al., 2004), or for more complex polymineralic argillaceous rocks (Van Loon et al., 2004; García-Gutiérrez et al., 2006; Xiang et al., 2013; Gimmi et al., 2014; Jacops et al., 2017). For these latter, the presence of elongated non-clay grains can provide additional contribution to the overall anisotropy in the water diffusion tensor (Robinet et al., 2012).

4. Summary and conclusions

The results described in the present study further confirm the significant role played by the preferred orientation of the particles on the diffusional properties of water in compacted porous media made of clay minerals. The originality of this work is provided by a close connection between experiments and simulations on representative virtual porous media, allowing quantitative agreement between the measured and calculated D_α/D_0 values. It is worth pointing out that such an agreement conceals significant differences in the probed spatial and dynamical domains between the experiments (~5 mm; 20 ms) and simulations (~4 µm; 4 ms). Accordingly, the spatial heterogeneity in the porosity and anisotropy within the samples at higher length scales are not accounted for in the computed VPM used here, or are just averaged in such a limited volume. Moreover, the flexibility of the clay particles (Honorio et al., 2018) and the interfacial molecular forces on the dynamics of the water molecules are not considered in the present study in these mesoscopic simulations. Despite these limitations and in line with previous computational studies (Tyagi et al., 2013; Bacle et al., 2016), the simulated VPM can be considered good toy models for estimating the underlying parameters of the pore network controlling the geometric parameter G (i.e., distribution in size, shape, orientation, and

connectivity of pores). This estimation is achieved in the present study based on the computation of the shape and the mean orientation of the particles, two parameters that are easily obtained experimentally. The validation of the computational methodology provides quantitative information on the role played by the preferred orientation of the particles on the G values, as a variation by a factor up to ~2 of D_α/D_0 for ε=0.5±0.02 is observed when increasing the anisotropy in the particle orientation. Because the order parameter $\langle P_2 \rangle$ values can significantly vary in compacted materials made from clay minerals (Perdigon-Aller et al., 2005; Méheust et al., 2006; Perdigón et al., 2007; Lutterotti et al., 2010; Carrier et al., 2016), this parameter undoubtedly deserves, as a porosity parameter, particular attention in the scope of predicting the macroscopic transport properties in compacted clay media. A logical continuation of this work could be, then, to expand the analysis of the influence of the preferred orientation on the water diffusion for different ε values. Using the same strategy combining experiments and simulations, another perspective could be to extend the analysis to other types of clay minerals, in particular to swelling clay minerals, leading to the presence of different type of porosities, and evaluating the overall diffusional properties of water.

Acknowledgements

The results presented are part of the Ph.D. thesis of T.D. granted by "Région Nouvelle-Aquitaine", University of Poitiers, France. Claude Veit (IC2MP, Poitiers, France) is thanked for the design and conception of the compaction and centrifugation cells for the sample preparation. Claude Laforest (IC2MP, Poitiers, France) and Stephan Rouzière (LPS, Saclay, France) are also acknowledged for their technical assistance in the induration and polishing steps of the sample preparation and in the XRS measurements, respectively. Dr. Pascale Launois (LPS, Saclay, France) is thanked for constructive discussions about XRS measurements. The authors are grateful to the CNRS interdisciplinary "défi Needs" through its "MiPor" program (Project TRANSREAC) and the European Union (ERDF) and "Région

Nouvelle Aquitaine" for providing financial support for this study. Additional support from Région Centre (France) is thanked for the funding of the DSX100 Bruker spectrometer used in this study. The authors gratefully acknowledge the anonymous reviewers for their constructive comments.

References

Altmann, S., Tournassat, C., Goutelard, F., Parneix, J.-C., Gimmi, T., Maes, N., 2012. Diffusion-driven transport in clayrock formations. Appl. Geochem. 27, 463–478. https://doi.org/10.1016/j.apgeochem.2011.09.015

Aulin, C., Salazar-Alvarez, G., Lindström, T., 2012. High strength, flexible and transparent nanofibrillated cellulose–nanoclay biohybrid films with tunable oxygen and water vapor permeability. Nanoscale 4, 6622–6628. https://doi.org/10.1039/C2NR31726E

Backeberg, N.R., Iacoviello, F., Rittner, M., Mitchell, T.M., Jones, A.P., Day, R., Wheeler, J., Shearing, P.R., Vermeesch, P., Striolo, A., 2017. Quantifying the anisotropy and tortuosity of permeable pathways in clay-rich mudstones using models based on X-ray tomography. Sci. Rep. 7, 14838. https://doi.org/10.1038/s41598-017-14810-1

Bacle, P., Dufrêche, J.-F., Rotenberg, B., Bourg, I.C., Marry, V., 2016. Modeling the transport of water and ionic tracers in a micrometric clay sample. Appl. Clay Sci. 123, 18–28. https://doi.org/10.1016/j.clay.2015.12.014

Basser, P.J., Mattiello, J., Lebihan, D., 1994. Estimation of the Effective Self-Diffusion Tensor from the NMR Spin Echo. J. Magn. Reson. B 103, 247–254. https://doi.org/10.1006/jmrb.1994.1037

Bourg, I.C., Sposito, G., Bourg, A., 2006. Tracer diffusion in compacted, water-saturated bentonite. Clays Clay Miner. 54, 363–374.

Callaghan, P.T., 1991. Principles of nuclear magnetic resonance microscopy. Clarendon Press, Oxford.

Carrier, B., Vandamme, M., Pellenq, R.J.-M., Bornert, M., Ferrage, E., Hubert, F., Van Damme, H., 2016. Effect of water on elastic and creep properties of self-standing clay films. Langmuir 32, 1370–1379.

Cebula, D., Thomas, R., Middleton, S., Ottewill, R., White, J., 1979. Neutron diffraction from clay-water systems. Clays Clay Min. 27, 39.

Chaikin, P.M., Lubensky, T.C., 1995. Principles of condensed matter physics. Cambridge University Press, Cambridge.

Charlet, L., Alt-Epping, P., Wersin, P., Gilbert, B., 2017. Diffusive transport and reaction in clay rocks: A storage (nuclear waste, CO2, H2), energy (shale gas) and water quality issue. Adv. Water Resour., Tribute to Professor Garrison Sposito: An Exceptional Hydrologist and Geochemist 106, 39–59. https://doi.org/10.1016/j.advwatres.2017.03.019

Cotts, R.M., Hoch, M.J.R., Sun, T., Markert, J.T., 1989. Pulsed field gradient stimulated echo methods for improved NMR diffusion measurements in heterogeneous systems. J. Magn. Reson. 1969 83, 252–266. https://doi.org/10.1016/0022-2364(89)90189-3

Dabat, T., Mazurier, A., Hubert, F., Tertre, E., Grégoire, B., Dazas, B., Ferrage, E., 2018. Mesoscale Anisotropy in Porous Media Made of Clay Minerals. A Numerical Study Constrained by Experimental Data. Materials 11, 1972.

Davidson, P., Petermann, D., Levelut, A.-M., 1995. The measurement of the nematic order parameter by x-ray scattering reconsidered. J. Phys. II 5, 113–131. https://doi.org/10.1051/jp2:1995117

Ferrage, E., Hubert, F., Baronnet, A., Grauby, O., Tertre, E., Delville, A., Bihannic, I., Prêt, D., Michot, L.J., Levitz, P., 2018. Influence of crystal structure defects on the small-angle neutron scattering/diffraction patterns of clay-rich porous media. J. Appl. Crystallogr. 51.

Ferrage, E., Hubert, F., Tertre, E., Delville, A., Michot, L.J., Levitz, P., 2015. Modeling the arrangement of particles in natural swelling-clay porous media using three-dimensional packing of elliptic disks. Phys. Rev. E 91, 062210. https://doi.org/10.1103/PhysRevE.91.062210

Gaboreau, S., Robinet, J.-C., Pret, D., 2016. Optimization of pore-network characterization of a compacted clay material by TEM and FIB/SEM imaging. Microporous Mesoporous Mater. 224, 116–128. https://doi.org/10.1016/j.micromeso.2015.11.035

García-Gutiérrez, M., Cormenzana, J.L., Missana, T., Mingarro, M., Martín, P.L., 2006. Large-scale laboratory diffusion experiments in clay rocks. Phys. Chem. Earth Parts ABC, MIGRATION 2005, The 10th international conference on the chemistry and migration of actinides and fission products in the geosphere 31, 523–530. https://doi.org/10.1016/j.pce.2006.04.004

Gimmi, T., Leupin, O.X., Eikenberg, J., Glaus, M.A., Van Loon, L.R., Waber, H.N., Wersin, P., Wang, H.A.O., Grolimund, D., Borca, C.N., Dewonck, S., Wittebroodt, C., 2014. Anisotropic diffusion at the field scale in a 4-year multi-tracer diffusion and retention experiment – I: Insights from the experimental data. Geochim. Cosmochim. Acta 125, 373–393. https://doi.org/10.1016/j.gca.2013.10.014

Gunsteren, W.F. van, Berendsen, H.J.C., Rullmann, J.A.C., 1981. Stochastic dynamics for molecules with constraints. Mol. Phys. 44, 69–95. https://doi.org/10.1080/00268978100102291

Hansen, J.-P., McDonald, I.R., 1990. Theory of Simple Liquids. Elsevier.

Hassan, M.S., Villieras, F., Gaboriaud, F., Razafitianamaharavo, A., 2005. AFM and low-pressure argon adsorption analysis of geometrical properties of phyllosilicates. J. Colloid Interface Sci. 296, 614–623. https://doi.org/10.1016/j.jcis.2005.09.028

Hermans, P.H., Platzek, P., 1939. Beiträge zur Kenntnis des Deformationsmechanismus und der Feinstruktur der Hydratzellulose. Kolloid-Z. 88: 68. https://doi.org/10.1007/BF01518890

Honorio, T., Brochard, L., Vandamme, M., Lebée, A., 2018. Flexibility of nanolayers and stacks: implications in the nanostructuration of clays. Soft Matter 14, 7354–7367. https://doi.org/10.1039/C8SM01359D

Hubert, F., Bihannic, I., Prêt, D., Tertre, E., Nauleau, B., Pelletier, M., Demé, B., Ferrage, E., 2013. Investigating the anisotropic features of particle orientation in synthetic swelling clay porous media. Clays Clay Miner. 61, 397–415. https://doi.org/10.1346/CCMN.2013.0610501

Jacops, E., Aertsens, M., Maes, N., Bruggeman, C., Swennen, R., Krooss, B., Amann-Hildenbrand, A., Littke, R., 2017. The Dependency of Diffusion Coefficients and Geometric Factor on the Size of the Diffusing Molecule: Observations for Different Clay-Based Materials. Geofluids 2017.

Keller, L.M., Seiphoori, A., Gasser, P., Lucas, F., Holzer, L., Ferrari, A., 2014. The Pore Structure of Compacted and Partly Saturated MX-80 Bentonite at Different Dry Densities. Clays Clay Miner. 62, 174–187. https://doi.org/10.1346/CCMN.2014.0620302

667 Labarthet, F.L., Buffeteau, T., Sourisseau, C., 2000. Orientation Distribution Functions in
668 Uniaxial Systems Centered Perpendicularly to a Constraint Direction. Appl. Spectrosc.
669 54, 699–705. https://doi.org/10.1366/0003702001949951
670 Leu, L., Georgiadis, A., Blunt, M., Busch, A., Bertier, P., Schweinar, K., Liebi, M., Menzel,
671 A., Ott, H., 2016. Multiscale description of shale pore systems by scanning SAXS and
672 WAXS microscopy. Energy Fuels 30, 10282–10297.
673 https://doi.org/10.1021/acs.energyfuels.6b02256
674 Lutterotti, L., Voltolini, M., Wenk, H.-R., Bandyopadhyay, K., Vanorio, T., 2010. Texture
675 analysis of a turbostratically disordered Ca-montmorillonite. Am. Mineral. 95, 98–103.
676 Méheust, Y., Knudsen, K.D., Fossum, J.O., 2006. Inferring orientation distributions in
677 anisotropic powders of nano-layered crystallites from a single two-dimensional WAXS
678 image. J. Appl. Crystallogr. 39, 661–670. https://doi.org/10.1107/S002188980602766X
679 Mermut, A.R., Cano, A.F., 2001. Baseline studies of the clay minerals society source clays:
680 chemical analyses of major elements. Clays Clay Miner. 49, 381–386.
681 Perdigón, A.C., Clarke, S.M., Aston, M., 2007. Neutron diffraction study of the orientational
682 order in filter cakes made of kaolinite under laminar and turbulent cross-flow. J. Membr.
683 Sci. 298, 80–91. https://doi.org/10.1016/j.memsci.2007.04.002
684 Perdigon-Aller, A.C., Aston, M., Clarke, S.M., 2005. Preferred orientation in filtercakes of
685 kaolinite. J. Colloid Interface Sci. 290, 155–165.
686 https://doi.org/10.1016/j.jcis.2005.04.038
687 Porion, P., Ferrage, E., Hubert, F., Tertre, E., Dabat, T., Faugère, A.M., Condé, F., Warmont,
688 F., Delville, A., 2018. Water Mobility within Compacted Clay Samples: Multi-Scale
689 Analysis Exploiting 1H NMR Pulsed Gradient Spin Echo and Magnetic Resonance
690 Imaging of Water Density Profiles. ACS Omega 3, 7399–7406.
691 Porion, P., Mukhtar, M.A., Faugère, A.M., Pellenq, R.J.M., Meyer, S., Delville, A., 2003. Water
692 Self-Diffusion within Nematic Dispersions of Nanocomposites: A Multiscale Analysis
693 of 1H Pulsed Gradient Spin−Echo NMR Measurements. J. Phys. Chem. B 107, 4012–
694 4023. https://doi.org/10.1021/jp022161q
695 Porion, P., Rodts, S., Al-Mukhtar, M., Faugère, A.-M., Delville, A., 2001. Anisotropy of the
696 solvent self-diffusion tensor as a probe of nematic ordering within dispersions of
697 nanocomposites. Phys. Rev. Lett. 87, 208302.
698 Reinholdt, M.X., Hubert, F., Faurel, M., Tertre, E., Razafitianamaharavo, A., Francius, G., Prêt,
699 D., Petit, S., Béré, E., Pelletier, M., 2013. Morphological properties of vermiculite
700 particles in size-selected fractions obtained by sonication. Appl. Clay Sci. 77, 18–32.
701 https://doi.org/10.1016/j.clay.2013.03.013
702 Robinet, J., Sardini, P., Coelho, D., Parneix, J., Prêt, D., Sammartino, S., Boller, E., Altmann,
703 S., 2012. Effects of mineral distribution at mesoscopic scale on solute diffusion in a
704 clay-rich rock: Example of the Callovo-Oxfordian mudstone (Bure, France). Water
705 Resour. Res. 48.
706 Sakharov, B., Drits, V., McCarty, D., Walker, G., 2016. Modeling Powder X-Ray Diffraction
707 Patterns of the Clay Minerals Society Kaolinite Standards: Kga-1, Kga-1b, and Kga-2.
708 Clays Clay Miner. 64, 314–333.
709 Sammaljärvi, J., Jokelainen, L., Ikonen, J., Siitari-Kauppi, M., 2012. Free radical
710 polymerisation of MMA with thermal initiator in brick and Grimsel granodiorite. Eng.
711 Geol. 135, 52–59.
712 Sato, H., Suzuki, S., 2003. Fundamental study on the effect of an orientation of clay particles
713 on diffusion pathway in compacted bentonite. Appl. Clay Sci. 23, 51–60.
714 Skare, S., Hedehus, M., Moseley, M.E., Li, T.-Q., 2000. Condition Number as a Measure of
715 Noise Performance of Diffusion Tensor Data Acquisition Schemes with MRI. J. Magn.
716 Reson. 147, 340–352. https://doi.org/10.1006/jmre.2000.2209

Stejskal, E.O., Tanner, J.E., 1965. Spin Diffusion Measurements: Spin Echoes in the Presence of a Time-Dependent Field Gradient. J. Chem. Phys. 42, 288–292. https://doi.org/10.1063/1.1695690

Suuronen, J.-P., Matusewicz, M., Olin, M., Serimaa, R., 2014. X-ray studies on the nano- and microscale anisotropy in compacted clays: Comparison of bentonite and purified calcium montmorillonite. Appl. Clay Sci. 101, 401–408. https://doi.org/10.1016/j.clay.2014.08.015

Suzuki, S., Sato, H., Ishidera, T., Fujii, N., 2004. Study on anisotropy of effective diffusion coefficient and activation energy for deuterated water in compacted sodium bentonite. J. Contam. Hydrol. 68, 23–37. https://doi.org/10.1016/S0169-7722(03)00139-6

Takahashi, H., Tachi, Y., 2019. 3D-microstructure analysis of compacted Na-and Cs-montmorillonites with nanofocus X-ray computed tomography and correlation with macroscopic transport properties. Appl. Clay Sci. 168, 211–222.

Tertre, E., Delville, A., Prêt, D., Hubert, F., Ferrage, E., 2015. Cation diffusion in the interlayer space of swelling clay minerals–A combined macroscopic and microscopic study. Geochim. Cosmochim. Acta 149, 251–267.

Tinnacher, R.M., Holmboe, M., Tournassat, C., Bourg, I.C., Davis, J.A., 2016. Ion adsorption and diffusion in smectite: Molecular, pore, and continuum scale views. Geochim. Cosmochim. Acta 177, 130–149. https://doi.org/10.1016/j.gca.2015.12.010

Tournassat, C., Steefel, C.I., 2015. Ionic Transport in Nano-Porous Clays with Consideration of Electrostatic Effects. Rev. Mineral. Geochem. 80, 287–329. https://doi.org/10.2138/rmg.2015.80.09

Tyagi, M., Gimmi, T., Churakov, S.V., 2013. Multi-scale micro-structure generation strategy for up-scaling transport in clays. Adv. Water Resour. 59, 181–195. https://doi.org/10.1016/j.advwatres.2013.06.002

Valleau, J., Diestler, D., Cushman, J., Schoen, M., Hertzner, A., Riley, M., 1991. Comment on: Adsorption and diffusion at rough surfaces. A comparison of statistical mechanics, molecular dynamics, and kinetic theory. J. Chem. Phys. 95, 6194–6195.

Van Loon, L.R., Mibus, J., 2015. A modified version of Archie's law to estimate effective diffusion coefficients of radionuclides in argillaceous rocks and its application in safety analysis studies. Appl. Geochem. 59, 85–94. https://doi.org/10.1016/j.apgeochem.2015.04.002

Van Loon, L.R., Soler, J.M., Müller, W., Bradbury, M.H., 2004. Anisotropic diffusion in layered argillaceous rocks: a case study with Opalinus Clay. Environ. Sci. Technol. 38, 5721–5728. https://doi.org/10.1021/es049937g

Wenk, H.-R., Kanitpanyacharoen, W., Voltolini, M., 2010. Preferred orientation of phyllosilicates: Comparison of fault gouge, shale and schist. J. Struct. Geol. 32, 478–489.

Wenk, H.-R., Voltolini, M., Mazurek, M., Van Loon, L.R., Vinsot, A., 2008. Preferred orientations and anisotropy in shales: Callovo-Oxfordian shale (France) and opalinus clay (Switzerland). Clays Clay Miner. 56, 285–306. https://doi.org/10.1346/CCMN.2008.0560301

Xiang, Y., Al, T., Scott, L., Loomer, D., 2013. Diffusive anisotropy in low-permeability Ordovician sedimentary rocks from the Michigan Basin in southwest Ontario. J. Contam. Hydrol. 155, 31–45. https://doi.org/10.1016/j.jconhyd.2013.09.002